

Raising the observed metallicity floor with a 3D non-LTE analysis of SDSS J102915.14+172927.9[★]

C. Lagae¹, A. M. Amarsi², L. F. Rodríguez Díaz³, K. Lind^{1,4}, T. Nordlander^{4,5}, T. T. Hansen¹ and A. Heger^{4,6}

¹ Department of Astronomy, Stockholm University, Albanova University Center, 106 91 Stockholm, Sweden
e-mail: cis.lagae@astro.su.se

² Theoretical Astrophysics, Department of Physics and Astronomy, Uppsala University, Box 516, SE-751 20 Uppsala, Sweden

³ Stellar Astrophysics Centre, Department of Physics and Astronomy, Aarhus University, Ny Munkegade 120, DK-8000 Aarhus C, Denmark

⁴ ARC Centre of Excellence for All Sky Astrophysics in 3 Dimensions (ASTRO 3D), Australia

⁵ Research School of Astronomy and Astrophysics, Australian National University, Canberra, ACT 2611, Australia

⁶ School of Physics and Astronomy, Monash University, Clayton, Vic 3800, Australia

Accepted 2 March 2023; Received 23 December 2022

ABSTRACT

Context. The first stars mark the end of the cosmic dark ages, produce the first heavy elements, and set the stage for the formation of the first galaxies. Accurate chemical abundances of ultra metal-poor stars ($[\text{Fe}/\text{H}] < -4$) can be used to infer properties of the first stars, and thus the formation mechanism for low-mass second generation stars in the early universe. Spectroscopic studies have shown that most second generation stars are carbon-enhanced. A notable exception is SDSS J102915.14+172927.9, the most metal-poor star known to date, largely by virtue of the low upper limits of the carbon abundance reported in earlier studies.

Aims. We reanalyse the composition of SDSS J102915.14+172927.9 with the aim to provide improved observational constraints on the lowest metallicity possible for low-mass star formation and constrain the properties of its Population III progenitor star.

Methods. We developed a tailored three dimensional (3D) model atmosphere for SDSS J102915.14+172927.9 with the Staggercode, making use of an improved surface gravity estimate based on the Gaia DR3 parallax. Snapshots from the model were used as input in the radiative transfer code Balder to compute 3D non-local thermodynamic equilibrium (non-LTE) synthetic spectra. These spectra were then used to infer abundances for Mg, Si, Ca, Fe and Ni, and upper limits on Li, Na and Al. Synthetic 3D LTE spectra were computed with Scate to infer the abundance of Ti and upper limits on C and N.

Results. In contrast to earlier works based on 1D non-LTE corrections to 3D LTE results, we are able to achieve ionisation balance for Ca I and Ca II when employing our consistent 3D non-LTE treatment. The elemental abundances are systematically higher than those found in earlier works. In particular, $[\text{Fe}/\text{H}]$ is increased by 0.57 dex, and the upper limits of C and N are larger by 0.90 dex and 1.82 dex, respectively.

Conclusions. We find that Population III progenitors with masses $10\text{--}20 M_{\odot}$ exploding with energy $E \lesssim 3 \cdot 10^{51}$ erg can reproduce our 3D non-LTE abundance pattern. Our 3D non-LTE abundances are able to better constrain the progenitor mass and explosion energy as compared to our 1D LTE abundances. Contrary to previous work, we obtain higher upper limits on the carbon abundance that are “marginally consistent” with star formation through atomic line cooling, and as such, prevent strong conclusions about the formation mechanism of this low mass star.

Key words. Atomic processes — Radiative transfer — Stars: atmospheres — Stars: abundances — Stars: Population II — Stars: Population III

1. Introduction

The first stars (Population III stars, hereafter Pop III stars) in our universe formed directly from Big Bang nucleosynthesis products: H, He and traces of Li. These stars were the source of the first enrichment of the interstellar and intergalactic medium, and set the stage for the formation of the first galaxies and started the epoch of reionisation (Bromm & Yoshida 2011).

Despite their importance, the details of star formation and the resulting initial mass function (IMF) of Pop III stars are still uncertain. Initial studies suggested that the lack of metals in star-forming clouds caused the absence of an efficient cooling mechanism and suppressed the formation of low-mass stars in the early universe. Hydrodynamic simulations based on cooling by hy-

drogen molecules predicted stellar masses larger than $> 100 M_{\odot}$ (Bromm & Yoshida 2011). More recent studies that incorporate longer timescales, higher resolution, and improved physics such as subsonic turbulence (Clark et al. 2011a), fragmentation of accretion disks (Greif et al. 2011; Clark et al. 2011b), protostellar radiation feedback (Hosokawa et al. 2011, 2016; Hirano et al. 2014), multiplicity (Stacy & Bromm 2013), and a combination of these (Susa 2013; Susa et al. 2014; Stacy et al. 2016) allow stars to form with initial masses of several solar masses from $\lesssim 1 M_{\odot}$ up to $1000 M_{\odot}$. The lack of direct observations of Pop III stars and expected scarcity of long-lived low-mass ($M \lesssim 0.8 M_{\odot}$) Pop III stars in the galaxy (Hartwig et al. 2015; Magg et al. 2019), however, makes it difficult to directly constrain these predictions.

One way to indirectly study the properties of the first stars is to look at metal-poor second-generation stars (Population II

[★] Based on observations obtained at ESO Paranal Observatory, programme 286.D-5045, P.I. P. Bonifacio.

stars). These stars are born from the gas that the Pop III stars enrich; moreover, studies claim that stars with metallicity of up to $[\text{Fe}/\text{H}] < -3$ could, in principle, be formed from a cloud enriched by a single supernova (Tominaga et al. 2007; Nomoto et al. 2013; Keller et al. 2014; Frebel & Norris 2015). Using a semi-analytical model of early universe star formation, Hartwig et al. (2018) found that 40% of stars with $-6 \lesssim [\text{Fe}/\text{H}] \lesssim -4$ are enriched by only one nucleosynthesis event (mono-enriched). Therefore, by comparing the chemical compositions of ultra metal-poor stars (UMP, $[\text{Fe}/\text{H}] < -4$, Beers & Christlieb 2005) to theoretical yields of first-star core-collapse supernovae, it is, in principle, possible to constrain the explosion properties and IMF of the first stars – at least for single stars, although some questions about asymmetric supernovae and dilution remain (Ezzeddine et al. 2019; Magg et al. 2020). These types of analyses indicate that the progenitors of Pop II stars typically have stellar masses in the range of $10 - 100 M_{\odot}$ (Lai et al. 2008; Heger & Woosley 2010; Joggerst et al. 2010; Ishigaki et al. 2014, 2018; Tominaga et al. 2007, 2014; Placco et al. 2015).

A related problem concerns the transition from Pop III star formation to low-mass star formation that follows the currently known IMF peaking at $\sim 0.2 - 0.3 M_{\odot}$ (Kroupa 2002; Chabrier 2003; Bastian et al. 2010). Two models have been proposed for this transition to predominantly low-mass star formation: atomic fine-structure line cooling (Bromm & Loeb 2003) and dust-induced fragmentation (Schneider et al. 2003; Omukai et al. 2005; Ji et al. 2014). Atomic fine-structure line cooling can occur if the gas is enriched beyond critical abundances of C II and O I, often approximated as $Z_{\text{crit}}/Z_{\odot} \sim 10^{-3.5}$. On the other hand, dust-induced fragmentation which requires dust formation in the ejecta from first star supernovae, can already operate at critical abundances that are a factor $10 - 100$ smaller: $Z_{\text{crit}}/Z_{\odot} \sim 10^{-5}$ (Omukai et al. 2005; Schneider et al. 2012a).

In the last decade, multiple large spectroscopic surveys have expanded our sample of ultra metal-poor stars allowing us to make a first classification (Beers et al. 1985; Beers & Christlieb 2005; Christlieb et al. 2008). One result of this work is that the fraction of carbon-enhanced metal-poor (CEMP, $[\text{C}/\text{Fe}] > 0.7$; Aoki et al. 2007 and Beers & Christlieb 2005) stars increases for decreasing metallicity (Placco et al. 2014; Arentsen et al. 2022). Below $[\text{Fe}/\text{H}] < -4.5$ we almost exclusively observe CEMP-stars. Due to their carbon-enhanced nature, these stars all obey the critical abundance necessary for atomic line cooling.

There is one notable exception: SDSS J102915.14+172927.9, hereafter “SDSS J102915+172927” (Caffau et al. 2011). This is the star with the lowest metal-mass fraction Z , currently known, in large parts due to a low upper limit on its carbon abundance: $[\text{C}/\text{H}] \leq -4.5$. Its low carbon abundance puts the star below the critical abundance for metal-line cooling, providing support for the dust-induced formation model (Caffau et al. 2012; Schneider et al. 2012b; Klessen et al. 2012).

Inferences about the Pop III progenitors and about the Pop II formation mechanism, however, rely on stellar chemical abundances that are determined via high-resolution spectroscopy. These analyses are strongly sensitive to the approximations employed when modelling the synthetic spectra. The abundance offsets introduced by the simplifying assumptions of one dimensional (1D) hydrostatic atmospheres and local thermodynamic equilibrium (LTE) have been shown to be particularly severe at lower metallicities (Amarsi et al. 2016b, 2022; Bergemann et al. 2012, 2019; Ezzeddine et al. 2017).

One source of these discrepancies is that, contrary to 3D simulations wherein convection arises naturally, in 1D hydrostatic

models convection must be treated in an approximate way, for example by the mixing-length theory (Böhm-Vitense 1958). The 1D models also cannot make predictions on other intrinsic 3D hydrodynamic effects such as granulation and cooling by adiabatic expansion. The first 3D models of metal-poor stellar atmospheres showed that the absence of adiabatic cooling in 1D models leads to a severe overestimation of the surface temperature stratification (Stein & Nordlund 1998; Asplund et al. 2005). Hence, in LTE, 3D synthetic spectral lines of neutral species that are formed in these surface layers are often stronger than their 1D counterparts. Equally important, non-LTE effects for minority species subject to overionisation are expected to be larger in the steeper temperature gradients of metal-poor stars (Bergemann et al. 2012). To mitigate the problems, without attempting fully consistent 3D non-LTE synthesis, estimates of non-LTE and 3D effects have often been made separately as in the case for SDSS J102915+172927 (Caffau et al. 2011, 2012). The non-LTE effects, however, in fact vary across the surface due to horizontal inhomogeneities (Asplund et al. 2003; Nordlander et al. 2017). Hence attempting to correct for 3D and non-LTE effects separately, often leads to new abundance offsets. Nordlander et al. (2017) already showed that doing a full 3D non-LTE spectral synthesis of SMSS0313-6708, the most iron-poor star currently known, can significantly change abundance estimates. The full 3D non-LTE analysis increased the upper limit on the Fe abundance for this star to $[\text{Fe}/\text{H}] < -6.53$ as compared to the previous non-LTE upper limit $[\text{Fe}/\text{H}] < -7.52$ computed using averaged 3D ((3D)) model atmospheres (Bessell et al. 2015). Additionally, recent work on C and O (Amarsi et al. 2016a), Li (Wang et al. 2021), and Fe (Amarsi et al. 2016b, 2022) also demonstrated significant 1D LTE – 3D non-LTE abundance corrections for metal-poor stars.

In light of recent advancements in the field of modelling 3D model atmospheres and 3D non-LTE spectral synthesis, we perform for the first time a fully consistent 3D non-LTE abundance analysis of the most metal-poor star SDSS J102915+172927. In §2 we present the model atmosphere, radiative transfer and model atoms used to produce 3D non-LTE synthetic spectra. The resulting abundances are presented in §3 and discussed in §4; our conclusions given in §5.

2. Method

2.1. Observational data and stellar parameters

Observational spectra of SDSS J102915+172927 ($G = 16.5$, Gaia Collaboration 2020) were obtained by the programme 286.D-5045 and principle investigator P. Bonifacio, using the UVES spectrograph (Dekker et al. 2000) mounted on the VLT. More information about the instrument settings and other details of the observations can be found in Caffau et al. (2012). For this work, we downloaded the reduced science spectra containing 14 individual exposures of 3005 s each from the ESO advanced data product archive¹. We find a signal-to-noise ratio per pixel of approximately 35 at 650 nm for each individual exposure, which agrees with the values found by Caffau et al. (2012). Each exposure was aligned manually by adding a radial velocity shift such that the cores of the H Balmer lines and the Ca II-doublet corresponded to the correct central wavelength. Subsequently, co-adding all exposures resulted in the final spectrum with a signal-to-noise ratio per pixel of $S/N \approx 20$ in the blue region around

¹ Url: http://archive.eso.org/eso/eso_archive_main.html

3500 Å, ≈ 70 around the green region 5200 Å and ≈ 35 in the red region at 8500 Å of the spectrum.

Caffau et al. (2012) determined the stellar effective temperature (T_{eff}) from the $(g - z)$ colour obtained by Ludwig et al. (2008), resulting in a value of 5811 ± 150 K. For the surface gravity, it was still unclear at the time of the original analysis whether SDSS J102915+172927 is a dwarf or a subgiant star. Caffau et al. (2012) determined a gravity of $\log g = 4.0 \pm 0.5$ dex, but not excluding a higher gravity of ≈ 4.5 dex. With the release of an improved parallax by Gaia DR2 $\varpi = 0.734 \pm 0.07$ mas, Bonifacio et al. (2018) resolved the gravity issue by comparing metal-poor isochrones from A. Chieffi (Priv. Comms.) to their newly computed absolute V -magnitude using Gaia DR2 data, concluding that SDSS J102915+172927 is a dwarf star. Sestito et al. (2019) computed $T_{\text{eff}} = 5764 \pm 60$ K and $\log g = 4.7 \pm 0.1$ dex by fitting MESA isochrones, with $[\text{Fe}/\text{H}] = -4$, to observations using Gaia DR2 astrometric and photometric data. The estimated error of using isochrones with a fixed metallicity for stars that are more metal poor than $[\text{Fe}/\text{H}] = -4$ is expected to be small and accounted for by adding an additional error of 0.01 mag to the photometric uncertainties (Sestito et al. 2019). Using the parallax from Gaia DR3 $\varpi = 0.648 \pm 0.06$ mas, Sestito (Priv. Comms.) arrived at $T_{\text{eff}} = 5811 \pm 51$ K and $\log g = 4.68 \pm 0.1$ dex. This effective temperature compares well to the original derived value whereas the surface gravity is 0.7 dex higher but corresponds to SDSS J102915+172927 being a dwarf star. In this work we used the latest values derived by Sestito (Priv. Comms.) using Gaia DR3 data.

2.2. Model atmosphere

The tailored 3D “box-in-a-star” model atmosphere was computed for this work by using the radiative-hydrodynamic Stagger-code (Nordlund & Galsgaard 1995; Nordlund et al. 2009), with later improvements by its user community (Magic et al. 2013; Collet et al. 2018). Stagger solves the fluid conservation equations (mass, energy, momentum) on a staggered Eulerian mesh and radiation is included as heating and cooling terms in the energy conservation equation. The size of the box is chosen such that it contains roughly ten granules and covers the top of the convective zone, superadiabatic region, photosphere and upper layers of the atmosphere. The surface gravity is fixed since the box only represents a small region of the star. The radiative transfer is solved in LTE, where the scattering contribution is included in the total extinction, using an approximate opacity binning method (Nordlund 1982; Skartlien 2000; Ludwig & Steffen 2013; Collet et al. 2018) with 12 bins. Since computing the full monochromatic solution in 3D is computationally unfeasible, all wavelength points are sorted in 12 bins according to their formation depth $\tau_{\text{Ross}}(\tau_{\lambda} = 1)$. For each bin a mean opacity κ_i , containing both continuum and line opacity, is computed that is subsequently used in the calculation of the mean intensity and radiative heating rate:

$$q_{\text{rad}} = 4\pi\rho \sum_i \kappa_i (J_i - B_i), \quad (1)$$

with density ρ , J_i the mean intensity for bin i and B_i the Planck function at the local gas temperature. More details of the implementation in Stagger can be found in Magic et al. (2013). The Equation of State (EOS) is a customised version from Mihalas et al. (1988) constructed by Trampedach et al. (2013), which includes the following species: H, He, C, N, O, Ne, Na, Mg, Al, Si, S, Ar, K, Ca, Cr, Fe, Ni, H₂, and H₂⁺. Continuous absorption

and scattering coefficients are taken from Hayek et al. (2010) and line opacities from Gustafsson et al. (2008).

Surface gravity, metallicity, bottom boundary entropy and a fiducial hyper-viscosity parameter are the only free parameters in the Stagger simulations, with effective temperature being an emergent property. As such, the surface gravity was fixed to the value selected in §2.1 and metallicity at $[\text{Fe}/\text{H}] = -4$ with alpha-enhancement $[\alpha/\text{Fe}] = 0.4$ typical for stars at these low-metallicities (Mashonkina et al. 2017). The bottom boundary entropy was modified iteratively in order to obtain the desired effective temperature of ~ 5811 K. The H to He abundance ratio is fixed at solar value while the other elemental abundance ratios with respect to H are scaled down from their solar values, for example $[\text{C}/\text{H}] = -4$ and $[\text{N}/\text{H}] = -4$ using solar abundances from Asplund et al. (2009). A summary of the input and emergent stellar parameters of the computed model are given in Table 1 together with literature estimates. The model itself is set on a $240 \times 240 \times 240$ Cartesian grid that is more spatially refined near the surface to resolve the steep photospheric temperature gradient. Information about the numerical details of the code can be found in Magic et al. (2013) and Collet et al. (2018).

In addition to the tailored 3D model atmosphere, a MARCS atmosphere, interpolated from the MARCS grid (Gustafsson et al. 2008), was used to compute 1D abundances. The 1D plane-parallel atmosphere has a metallicity of $[\text{Fe}/\text{H}] = -4$ with similar α , C, N, and O abundances as the Stagger model and microturbulence of 1 km/s. The exact value of the microturbulence was relaxed for the post-processing spectrum synthesis described in §2.3. A comparison between the 1D MARCS and 3D Stagger model is made in Fig. 1, where the temperature stratification of both is displayed together with the average stratification of the 3D model ($\langle 3D \rangle$). This average is calculated by taking the mean temperature of all vertical cross-sections at each depth point in optical depth space. It showcases the impact of adiabatic cooling in 3D metal-poor atmospheric models in the upper atmosphere where the temperature structure differs significantly compared to the 1D model. The 3D model has a steeper temperature gradient at the photosphere. Although the $\langle 3D \rangle$ -model is an improvement over the 1D model as it accurately describes the temperature stratification of the full 3D model, it loses information on the surface granulation and accompanying impact on spectral line formation.

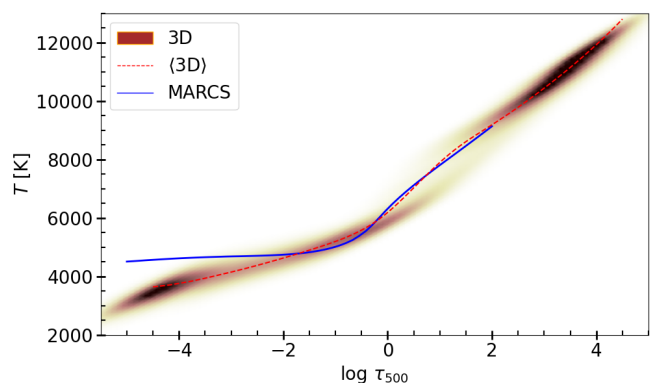


Fig. 1. Temperature heatmap of the Stagger model with its corresponding average ($\langle 3D \rangle$) of all vertical columns over optical depth (red dashed). The 1D MARCS temperature stratification is shown in blue.

Table 1. Summary of the stellar parameters of SDSS J102915+172927 obtained in previous literature studies and for the hydrodynamic models used in this work.

	T_{eff} [K]	$\log g$ [dex]	[Fe/H]
Caffau et al. (2012)	5811 ± 150	4.0 ± 0.5	-4.89 ± 0.10
Sestito et al. (2019) & Gaia DR2	5764 ± 56	4.69 ± 0.1	...
F. Sestito ² & Gaia DR3	5811 ± 51	4.68 ± 0.1	...
Stagger 3D model atmosphere	≈ 5810	4.70	-4
MARCS 1D model atmosphere	5811	4.68	-4

² Private communication

2.3. Spectral modelling

The radiative transfer code *Balder* was used to compute 1D and 3D non-LTE synthetic line profiles for the elements for which we have suitable atomic models: Si (Amarsi & Asplund 2017), Li (Wang et al. 2021), Ca, Mg (Asplund et al. 2021), Na (Lind et al. 2011), Al (Nordlander & Lind 2017) and Fe (Amarsi et al. 2016b, 2022; Lind et al. 2017). The code itself is based upon the original framework of *Multi3D* (Leenaarts & Carlsson 2009). Amarsi et al. (2016a,b) expanded the original code, in particular with an improved opacity package *BLUE*, change in angle quadrature and implementation of frequency parallelisation.

Balder solves the statistical equilibrium for user-specified trace elements using the multilevel approximate lambda iteration pre-conditioning method of Rybicki & Hummer (1992) on a Cartesian grid. The assumption is made that any deviations from LTE do not impact the temperature stratification or the densities of other elements. The Equation of State, background, and line opacities are treated by the *BLUE* package (Amarsi et al. 2016b), in which the latter is precomputed on a grid of wavelength, density and temperature. To decrease the computational cost of the 3D calculations, the resolution of the *Stagger* model was reduced to 60 grid points in the horizontal and 101 points in the vertical direction. Nordlander et al. (2017) showed that this mesh reduction impacts the derived abundances by at most 0.03 dex. For the 3D spectral synthesis, we sampled the temporal variation of the atmosphere by computing line strengths from three different snapshots of the *Stagger* model. These were chosen so as to maximise the difference in T_{eff} and, therefore, the difference in resulting line profiles. We find mean abundance variations between snapshots of no more than 0.02 dex, which is in line with similar work done by Nordlander et al. (2017).

For the other elements that we do not expect large deviations from non-LTE (Ti II; Mallinson et al. 2022), or for which we do not have the atomic and molecular data needed to solve the statistical equilibrium equations (Ni I, CH and NH), we compute 1D and 3D LTE synthetic spectra using *Scate* (Hayek et al. 2011). The necessary atomic line data (oscillator strengths, excitation potential and damping parameters) are taken from Kurucz (2016) for Ti II and Kurucz (2008) for Ni I, using the VALD database (Piskunov et al. 1995; Ryabchikova et al. 2015).

A range of synthetic spectra were calculated with varying abundances ($\Delta = 0.2$ dex) for the elements: Li I, CH, NH, Na I, Al I, Mg I, Si I, Ca I, Ca II, Ti II, Fe I and Ni I, also listed in Table 3. These were interpolated to the equivalent width (W_λ) measured in the observed spectrum. The latter is found by fitting one or more, in the case of blended lines, Gaussians to the observed line profiles. An overview of the identified spectral lines and cor-

responding equivalent widths is given in Table B.1. Caffau et al. (2012) report the equivalent widths for a selection of lines in their Table 4, all of which agree with our values within their error. For the elements with no visible lines in the UVES spectrum (Li, Na, Al, CH, and NH), upper limits were estimated using either Cayrel’s formula (Cayrel 1988; Cayrel et al. 2004, for Li, Na and Al) or a reduced χ^2 statistical test (CH and NH). In the second case we applied artificial broadening to the synthetic spectra to simulate instrumental broadening with a resolution of 38 000. Further details on the upper limit determination are given in the respective results section of Li (§3.1) and C (§3.2).

Spectrum synthesis calculations in 1D contain microturbulent velocity v_{mic} as an extra free broadening parameter to approximate the convective velocity fields. This free parameter is usually determined by flattening the abundances of individual Fe I and Fe II lines as a function of reduced equivalent width W_λ/λ_0 . Since we only detect Fe I in the observed spectrum, we computed 1D (non-)LTE Fe I abundances for three different values of microturbulence $v_{\text{mic}} = 1, 1.5$ and 2 km/s to obtain a final best fitting value of $v_{\text{mic}} = 1.48 \pm 0.25$ km/s. The result of this analysis is shown in Fig. 2 where all detected Fe I lines are used to determine v_{mic} . This value is consistent with the empirical analysis performed by Frebel et al. (2013), for a star with $\log g = 4.7$. In all subsequent spectral synthesis computations a value of $v_{\text{mic}} = 1.5$ km/s was used.

The stipulated abundance errors originate from manually placing the continuum and from the noise of the spectrum. It is calculated from Cayrel’s formula (Cayrel 1988; Cayrel et al. 2004), which gives an error on the equivalent width that propagates through to the abundance error, with a separate contribution from the continuum placement. In addition, there is an error coming from the uncertainties on T_{eff} , $\log g$ and v_{mic} , which are computed by shifting one stellar parameter at a time in the MARCS atmosphere and performing an abundance analysis as described above. The error is then equal to the abundance offset between the new model and the model with correct stellar parameters. For example, the Mg I abundance increases by 0.08 dex when computed using a MARCS atmosphere with a T_{eff} that is 100 K hotter. These results are summarised in Table 2. Finally, the total error becomes:

$$\sigma_{\text{tot}}^2 = \sigma_{\text{Cayrel}}^2 + \sigma_{\text{continuum}}^2 + \sigma_{T_{\text{eff}}, \log g, v_{\text{mic}}}^2 \quad (2)$$

$$\text{with } \sigma_{\text{continuum}} = \frac{1}{S/N} \cdot W_\lambda.$$

Table 2. 1D (non-)LTE abundance ($A(X)$, see Eq. 3) sensitivity to the uncertainties on T_{eff} , $\log g$ and v_{mic} .

Species	$T_{\text{eff}} + 100 \text{ K}$	$T_{\text{eff}} - 100 \text{ K}$	$\log g + 0.2 \text{ dex}$	$\log g - 0.2 \text{ dex}$	$v_{\text{mic}} + 0.5 \text{ km/s}$	$v_{\text{mic}} - 0.5 \text{ km/s}$
Mg I	0.08	-0.09	-0.02	0.05	-0.01	0.01
Ca I	0.09	-0.09	-0.01	0.05	-0.01	0.01
Ca II	-0.04	-0.12	-0.03	-0.12	-0.06	0.08
Si I	0.07	-0.10	-0.01	0.01	-0.01	0.01
Fe I	0.10	-0.11	0.01	0.05	-0.02	0.03
Ti II	0.07	-0.05	0.08	-0.06	-0.07	0.09
Ni I	0.11	-0.10	0.01	0.02	-0.04	0.07
C	0.15	-0.15	-0.05	0.05	≈ 0	≈ 0
N	0.15	-0.15	-0.15	0.05	≈ 0	≈ 0
Li I	0.08	-0.07	0.01	0.03	≈ 0	≈ 0
Na I	0.07	-0.06	0.01	0.02	≈ 0	≈ 0
Al I	0.07	-0.08	-0.01	0.04	≈ 0	≈ 0

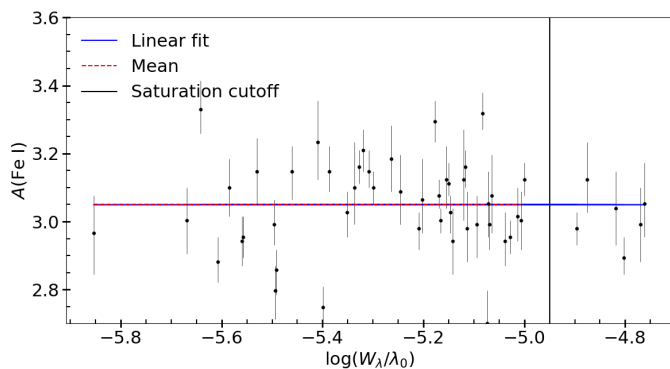


Fig. 2. 1D non-LTE Fe I abundances for each visible line in the spectrum interpolated to a microturbulence of $v_{\text{micro}} = 1.48 \text{ km/s}$. The *blue line* shows the best linear fit through the data while the *red dashed line* denotes the mean non-LTE abundance. The *black solid line* denotes the cutoff in reduced equivalent width between saturated and non-saturated lines: $\log[W_{\lambda}/\lambda_0] < -4.95$.

3. Results

All abundance results are summarised in Table 3 in the form:

$$A(X) = \log(x) + A(\text{H}), \quad (3)$$

where x is the number fraction of element X and $A(\text{H}) = 12$. Whenever an abundance is converted to the solar normalised abundance: $[X/\text{H}] = A(X) - A(X)_{\odot}$, we used the solar abundances from [Asplund et al. \(2021\)](#).

3.1. Lithium

The Li I line at 6707.6 \AA is not detected in the UVES spectrum such that we could only determine an upper limit. We used Cayrel’s formula ([Cayrel 1988](#)), similar to [Caffau et al. \(2012\)](#), to determine a 3σ upper limit. The resulting 3D non-LTE upper limit, $A(\text{Li}) < 1.06 \pm 0.05$, is slightly higher than the original value, $A(\text{Li})_{\text{Caffau+12}} < 0.9$, but still well below the Spite plateau, $A(\text{Li})_{\text{Spite}} \sim 2.2$ ([Spite & Spite 1982](#); [Sbordone et al.](#)

[2010](#); [Meléndez et al. 2010](#)), implying that the star has undergone significant Li depletion, as expected based on its effective temperature.

3.2. Carbon and nitrogen

Both C and N are undetected in the UVES spectrum, but the quality of the spectrum allows the calculation of robust upper limits. To obtain these, we computed 1D and 3D LTE synthetic spectra of the CH G-band at 4300 \AA and the NH-band at 3360 \AA for a wide range of abundances $A(\text{C}) = 3.6 - 5.6$ and $A(\text{N}) = 2.4 - 6.0$ in steps of $\Delta = 0.2 \text{ dex}$. The upper limit was determined using a reduced χ^2 -statistic where we ‘fitted’ the synthetic spectral bands to the UVES spectrum. The null hypothesis is that our featureless observed spectrum can be fully described by the synthetic spectrum, meaning that both are indistinguishable. The upper limit is then defined as the synthetic spectrum with abundance $A(\text{C})$ that does not statistically describe the observed featureless spectrum.

We start by masking out the blended Ti II and Fe I line in the NH- and CH-band, respectively, and compute the reduced χ^2_{ν} for each synthetic spectrum:

$$\bar{\chi}_{\nu}^2 = \frac{1}{\nu} \sum_{\lambda} \left(\frac{F_{\text{obs}}(\lambda) - F_{\text{synth}}(\lambda)}{\sigma_{\text{continuum}}(\lambda)} \right)^2, \quad (4)$$

with ν the degrees of freedom equal to the number of wavelength points minus 1 and $\sigma_{\text{cont}} = S/N^{-1}$. For a significance level of $\alpha = 0.05$ we can look up the corresponding mean of the χ^2 -distribution: $\chi^2_{\nu, \alpha}/\nu$ ([Bognar 2021](#)), where the probability that a randomly chosen χ^2 from the distribution function will be greater than $\chi^2_{\nu, \alpha}$ is equal to the significance level, in this case 5%. It follows that the null hypothesis is rejected for synthetic models that have $\bar{\chi}_{\nu}^2 > \chi^2_{\nu, \alpha}/\nu$, either because the synthetic spectrum does not properly model the observed spectrum or due to a statistically improbable excursion of probability 5%. This means that the upper limit on the CH and NH abundance is equal to the synthetic spectrum for which $\bar{\chi}_{\nu}^2 = \chi^2_{\nu, \alpha}/\nu$, as any model with a higher abundance do not statistically describe the featureless

spectrum we observe. A visualisation of the $\bar{\chi}_v^2$ values used to determine the upper limits for C and N is shown in Figure A.1.

Using this method, we increase the upper limit significantly for both molecular bands: $A(\text{C}) = 4.86$ dex and $A(\text{N}) = 4.65$ dex, as compared to Caffau et al. (2012): $A(\text{C})_{\text{Caffau}} = 3.96$ dex and $A(\text{N})_{\text{Caffau}} = 2.83$ dex. The corresponding synthetic spectra are shown in Figs. 3 and 4 for N and C, respectively. In addition, the new and old upper limits on C are shown together with a subset of metal-poor stars from the SAGA database (Suda et al. 2008) in Fig. 5.

The large increase of the C and N upper limit can originate from multiple sources such as: changes in surface gravity, spectrum synthesis code, and atmosphere between the original and this work. In the case of the CH and NH upper limits, however, we believe that the main discrepancy is likely due to a difference in methodology when determining these limits. Caffau et al. (2012) show in their Figs. 6 and 7 the molecular bands for different abundances $A(\text{C}) = 4.65$, 6.00 and $A(\text{N}) = 3.60$, 5.40. From visual inspection, their $A(\text{C}) = 5.40$ spectrum corresponds well to our synthetic spectrum with $A(\text{C}) = 5.00$, which points towards a ~ 0.4 dex abundance difference originating from the difference in surface gravity, atmospheric model and spectrum synthesis code. We hypothesise that the remaining difference is due to a difference in methodology. It is not described in Caffau et al. (2012), however, how the upper limits are derived such that a more direct comparison can not be made.

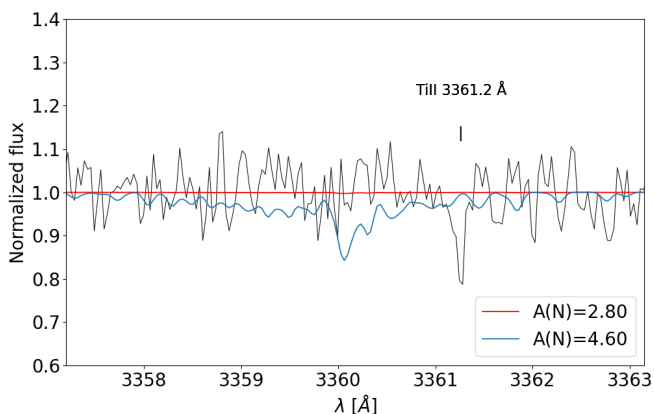


Fig. 3. The UVES spectrum (black) zoomed in on the NH-band at 3360 Å. The synthetic spectrum corresponding to the upper limit derived in this work is shown in blue, while the upper limit from Caffau et al. (2012) is shown in red. The Ti III at 3361.2 Å was excluded from the χ^2 -analysis.

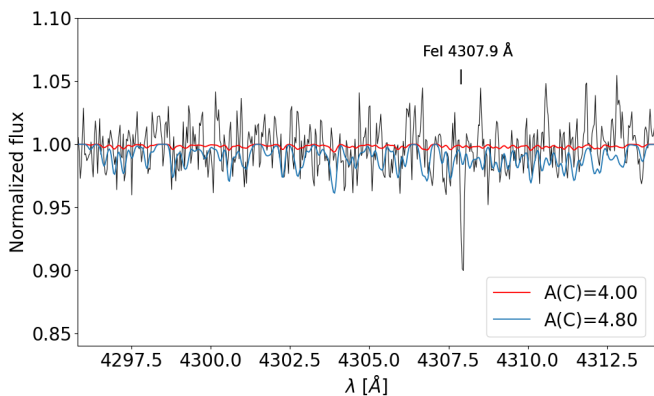


Fig. 4. CH G-band at 4300 Å. The Fe I at 4307.9 Å was excluded from the χ^2 -analysis.

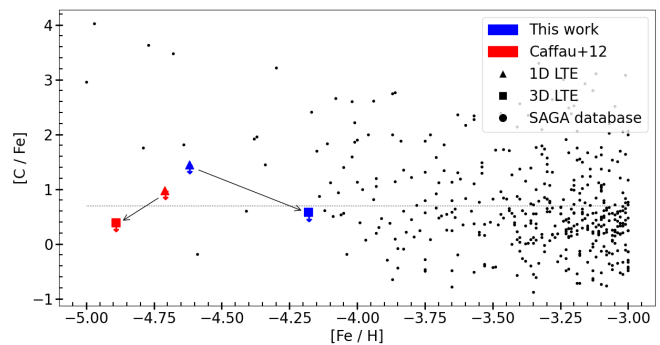


Fig. 5. Upper limits on $[\text{C}/\text{Fe}]$ for SDSS J102915+172927 in 1D LTE (triangles) and 3D LTE (squares) for both the original limits (Caffau et al. 2012, red), and the results of this work (blue). For comparison, we show the $[\text{C}/\text{Fe}]$ abundance for a sample of metal-poor stars from the SAGA database (Suda et al. 2008, black circles) and the cutoff for carbon-enhancement at $[\text{C}/\text{Fe}] = 0.7$ (dotted line) from Aoki et al. (2007)

3.3. Sodium and aluminium

No Na or Al absorption features could be identified in the spectrum. We therefore present upper limits for the two elements, in this star for the first time, at the Na I line at 5891.6 Å and Al I line at 3961.5 Å using the same method as for Li. The resulting 3σ -upper limits are shown in Table 3.

3.4. Alpha elements

Magnesium

We measured four Mg I lines which combine to a mean 3D non-LTE abundance of $A(\text{Mg}) = 3.18 \pm 0.05$ that is marginally consistent with Caffau et al. (2012), $A(\text{Mg}) = 3.06 \pm 0.12$. Sitnova et al. (2019) computed a 1D non-LTE value of $A(\text{Mg}) = 3.17 \pm 0.07$ using the updated surface gravity of $\log g = 4.7$.

Silicon

One Si I line was detected at 3905.5 Å for which we computed a 3D non-LTE abundance of $A(\text{Si}) = 3.42 \pm 0.12$ that is smaller as compared to Caffau et al. (2012), $A(\text{Si}) = 3.55 \pm 0.1$.

Calcium

One Ca I line was detected at 4226 Å together with the Ca II H&K lines and the Ca II triplet at ≈ 8500 Å. The Ca II H&K and the weakest line of the Ca II triplet were discarded due to being blended or too weak for a reliable equivalent width measurement. Using the resulting lines, we are able to recover ionisation balance between Ca I and Ca II in 3D non-LTE: $A(\text{Ca})_{\text{Ca I}} - A(\text{Ca})_{\text{Ca II}} = 0.01$ dex with a mean Ca abundance of $A(\text{Ca}) = 1.87 \pm 0.02$.

Caffau et al. (2012) obtained a 3D + non-LTE abundance of $A(\text{Ca})_{\text{Ca I}} = 1.76$ and $A(\text{Ca})_{\text{Ca II}} = 1.35$. Using an updated model atom, Sitnova et al. (2019) computed a 1D non-LTE Ca abundance, using similar stellar parameters as in this work, of $A(\text{Ca}) = 1.82 \pm 0.06$, where they fixed the Ca I/Ca II ionisation equilibrium to derive the surface gravity.

Titanium

We detected five Ti II lines in the UVES spectrum of which three were deemed strong enough to determine a reliable equivalent width. The resulting mean 3D LTE abundance $A(\text{Ti}) = 0.62 \pm 0.06$ is $+0.55$ dex higher than the original value derived by Caffau et al. (2012). A similar increase is seen in the 1D LTE case for which we obtain an abundance this is larger by $+0.39$ dex. Following Table 2 we can attribute approximately 0.2 dex to the change in surface gravity. The remaining 0.19 dex difference for the 1D LTE abundance can not be attributed to the different oscillator strengths used in this work, which are higher than the ones reported in Caffau et al. (2012, Table 4), leaving the origin of the discrepancy unknown.

3.5. Iron

The UVES spectrum contains 52 visible Fe I lines but no Fe II lines. For the abundance computation a cutoff in reduced equivalent width of $\log[W_\lambda/\lambda_0] < -4.95$ was used to remove lines that do not fall on the linear part of the curve-of-growth (Vickers 2000)². The remaining 46 Fe I lines are shown in Fig. 2 to the left of the solid black line. For the 1D LTE case we expect the only difference between our results and the one from Caffau et al. (2012) to be the change in gravity ($\Delta \log g = +0.7$ dex), as well as differences between the spectral synthesis codes and the model atmosphere employed. We obtain a value of $A(\text{Fe}) = 2.80 \pm 0.15$ that is comparable to the value found by Caffau et al. (2012), $A(\text{Fe}) = 2.87 \pm 0.13$. This result is assuring since Fe I is not strongly sensitive to surface gravity (see Table 2).

Our 1D non-LTE abundance, $A(\text{Fe}) = 3.05 \pm 0.13$, is comparable within its error to Caffau et al. (2012), $A(\text{Fe}) = 3.00 \pm 0.13$. In addition, Ezzeddine et al. (2017) recomputed the 1D non-LTE Fe abundance for this star, using a surface gravity of $\log g = 4.0$, and obtained a slightly higher value of $A(\text{Fe}) = 3.23 \pm 0.14$. They based their analysis only on three Fe I lines, however.

From our consistent 3D non-LTE analysis we derive an abundance of $A(\text{Fe}) = 3.28 \pm 0.13$ that is 0.57 dex higher than the 3D LTE + non-LTE value obtained by Caffau et al. (2012), $A(\text{Fe}) = 2.71 \pm 0.10$. We emphasise that Caffau et al. (2012) computed separate 1D non-LTE and 3D LTE abundance corrections and added these together to get a final 3D+non-LTE abundance. Applying a similar method to our abundances would yield a value of $A(\text{Fe})_{3\text{D}+\text{NLTE}} = 2.97 \pm 0.14$, which has a better agreement with Caffau et al. (2012), but significantly lower than the fully consistent 3D non-LTE result. Hence, this work demonstrates again that 3D and non-LTE effects influence each other non-linearly and cannot be simply added together for metal-poor stars.

This result supports the claim by Amarsi et al. (2016b) that metallicities of the most-metal poor stars are often systematically underestimated. This is because for Fe I lines, the non-LTE effects and the 3D effects tend to go in the same direction, and can enhance each other in warm metal-poor stars.

3.6. Nickel

We detected nine usable Ni I lines in the UVES spectrum for which we computed a mean 3D LTE abundance of $A(\text{Ni}) = 1.67 \pm 0.14$. This value is $+0.34$ dex higher than the original value. On the other hand, our 1D LTE abundance agrees to

within $+0.03$ dex with the value of Caffau et al. (2012), $A(\text{Ni}) = 1.65 \pm 0.14$.

4. Discussion

With our newly derived 3D non-LTE abundances, we can now address some of the questions regarding the properties of Pop III stars and low-mass star formation introduced in §1.

4.1. Supernova yield comparison

We compared our 3D non-LTE abundances with yields of core-collapse supernovae of non-rotating Pop III stars Heger & Woosley (2010), updated in 2012 for missing low-mass models³, using the StarFit code (Heger et al. 2023). Specifically, we used the Python version (0.17.12) of StarFit⁴ to find the best match between an input abundance pattern and supernova model employing a reduced χ^2 -algorithm ($\bar{\chi}^2$) (Heger & Woosley 2010, see their Section 7). Upper limits, however, are now treated by StarFit as in Eq. (6) of Magg et al. (2020) — they contribute to $\bar{\chi}^2$ similar to a measurement mismatch if violated and are basically ignored when well fulfilled. The one-dimensional mixing & fallback models (“*.S4.*”) cover the following range of progenitor star masses 9.6–100 M_\odot , as well as piston-driven explosion energies $E_{51} = 0.3$ –10 (with $E_{51} = 10^{51}$ erg) and hydrodynamic mixing fractions $f_{\text{mix}} = 0$ –0.25 (see Heger & Woosley 2010 for details). In addition, the fitting code employs a dilution factor f_{dil} that accounts for mixing of the supernova ejecta with the interstellar medium (Big Bang composition). This free parameter essentially shifts the whole supernova abundance pattern up or down. Li is excluded from the fitting procedure and C, N, Al, and Na are treated as upper limits. For Na and Al, more strict 1σ upper limits are calculated with Cayrel’s formula (Cayrel 1988; Cayrel et al. 2004), to use in the supernova fitting: $A(\text{Na})_{1\sigma} < 1.12 \pm 0.15$ and $A(\text{Na})_{1\sigma} < 1.54 \pm 0.15$.

The best fitting model has a progenitor mass of $M = 10.9 M_\odot$, an explosion energy of $E_{51} = 0.6$ and a mixing efficiency of $f_{\text{mix}} = 0.01$, and matches with $\bar{\chi}^2_{\text{best}} = 1.03$. The variance of the best-fitting models ($\bar{\chi}^2 < 3$) was analysed by selecting for each mass-energy pair the f_{mix} that has the lowest $\bar{\chi}^2$. The reasoning is that mixing acts as a free parameter in the one-dimensional explosion models. Moreover, the effect of mixing is small at masses $\sim 10 M_\odot$ and mainly affects elements with $Z > 20$ (Ca). The resulting distribution in mass and energy, and corresponding abundance patterns are shown in Fig. 6. We find that only a narrow range of progenitor masses, $M = 10$ –20 M_\odot , and explosion energies, $E_{51} = 0.3$ –3, are able to fit the abundance pattern of SDSS J102915+172927.

The difference between the best fit and yields from models with higher progenitor masses is shown in Fig. 7. At higher masses the supernova underproduces heavy elements (Ti, Fe, Ni) and overproduces Mg, Si, and Ca compared to the best fit model.

Applying the same fitting routine to our 1D LTE abundances results in a broader mass $M \approx 10$ –30 and energy range $E_{51} = 0.3$ –10 for all models with $\bar{\chi}^2 < 3$. This is explained by the lower 1D LTE Fe abundance that allows for models with higher progenitor mass to achieve good fits. Already in Fig. 7 it is noticeable that most supernova yields have lower Fe abundances than our 3D non-LTE result.

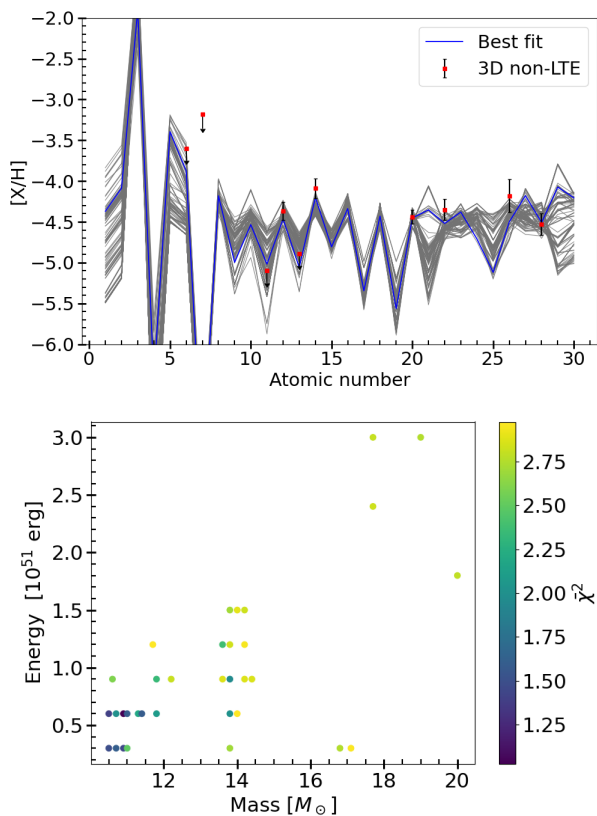
³ Data is available at <https://starfit.org>

⁴ Data and routines are available at <https://pypi.org/project/starfit/>

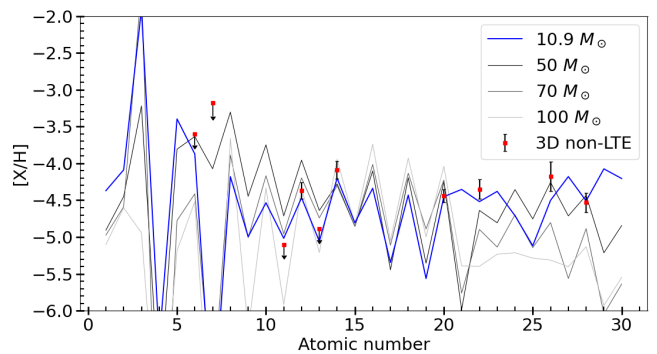
² Chapter “Stars, Spectroscopy of”, p.2199-2204, Figure 2

Table 3. Summary of the computed abundances ($A(X)$, see Eq. 3) and upper limits together with 3D+non-LTE values from Caffau et al. (2012).

Species	1D LTE	1D non-LTE	3D LTE	3D non-LTE	$[X/Fe]_{3D\ non-LTE}$	Caffau $_{3D+non-LTE}$
Mg I	2.90 ± 0.10	3.09 ± 0.09	2.93 ± 0.11	3.18 ± 0.11	-0.19	3.05 ± 0.12
Ca I	1.58 ± 0.13	1.72 ± 0.12	1.57 ± 0.10	1.88 ± 0.08	-0.24	1.79 ± 0.10
Ca II	2.14 ± 0.13	1.87 ± 0.14	1.96 ± 0.12	1.87 ± 0.11	-0.25	1.38 ± 0.09
Si I	3.16 ± 0.13	3.24 ± 0.12	3.20 ± 0.12	3.42 ± 0.12	0.09	3.56 ± 0.10
Fe I	2.80 ± 0.22	3.05 ± 0.20	2.70 ± 0.20	3.28 ± 0.19	...	2.63 ± 0.10
Ti II	0.54 ± 0.18	...	0.62 ± 0.13	...	-0.17	0.07 ± 0.16
Ni I	1.71 ± 0.22	...	1.67 ± 0.20	...	-0.38	1.33 ± 0.11^1
C	$< 5.25 \pm 0.14$...	$< 4.86 \pm 0.15$...	< 0.58	$< 3.96^1$
N	$< 5.13 \pm 0.18$...	$< 4.65 \pm 0.20$...	< 1.00	$< 2.83^1$
Li I, 3σ	$< 1.02 \pm 0.05$	$< 0.93 \pm 0.05$	$< 1.00 \pm 0.05$	$< 1.06 \pm 0.05$	< 1.99	< 0.90
Na I, 3σ	$< 1.55 \pm 0.10$	$< 1.48 \pm 0.10$	$< 1.58 \pm 0.15$	$< 1.62 \pm 0.15$	< -0.42	...
Al I, 3σ	$< 1.51 \pm 0.10$	$< 1.90 \pm 0.10$	$< 1.51 \pm 0.15$	$< 2.05 \pm 0.15$	< -0.20	...

¹ 3D LTE abundance from Caffau et al. (2012)

Fig. 6. The top panel shows the 3D non-LTE abundances (red squares) together with all supernovae models that have $\chi^2 < 3$ (solid grey lines), the best fit is shown in blue. The Bottom Panel show the progenitor mass and explosion energy for the same best-fitting models as shown in the Top Panel, together with their respective χ^2 values.

After the original discovery of SDSS J102915+172927, there have been several papers comparing its abundance pattern


Fig. 7. 3D non-LTE abundances from this paper (red squares) are shown together with the best fitting progenitor supernova-model in blue and three other models with a higher progenitor mass (grey): $M = 50, 70, 100 M_{\odot}$, $E_{51} = 0.3$ and $f_{mix} = 0.25$.

to theoretical yields of Pop III supernovae. The following literature results all use the original abundances from Caffau et al. (2012). Similar to this work, Placco et al. (2015) used the supernova models of Heger & Woosley (2010) to find a best fitting progenitor mass of $M = 10.6 M_{\odot}$ with explosion energy $E_{51} = 0.9$, which is in agreement with our work. Schneider et al. (2012b) used the Pop III core-collapse supernova models by Limongi & Chieffi (2012) to find a best fit for progenitors with mass $M = 20$ and $35 M_{\odot}$ and explosion energy $E_{51} = 1$. Tominaga et al. (2014) compared three core-collapse SNe models taken from Iwamoto et al. (2005); Tominaga et al. (2007) with varying mass (25 and $40 M_{\odot}$) and mixing efficiency with a sample of metal-poor stars including SDSS J102915+172927. Their best match is a progenitor star with $M = 25 M_{\odot}$ without mixing enhancement. Using the same Pop III supernova and hypernova models as Tominaga et al. (2014), Ishigaki et al. (2014) found a better agreement with a hypernova of $M = 40 M_{\odot}$, $E_{51} = 30$ and mixing $\log f = -0.9$, where they attribute the obtained explosion energy to the relatively high [Si/Ca] ratio. These papers find

a higher progenitor mass and explosion energy than this work. We note, however, that the data sets of [Iwamoto et al. \(2005\)](#) and [Tominaga et al. \(2007\)](#) only cover a comparably limited progenitor mass range. In summary, based on our new analysis and using the model set of [Heger & Woosley \(2010\)](#), we find that the observed abundance pattern of SDSS J102915+172927 can be well explained by a typical single star supernova (typical mass range 10–20 M_{\odot} and typical explosion energy, $E_{51} = 0.3 - 3$) of a compact Pop III star (low mixing, $f_{\text{mix}} = 0.01$, as compared to red super-giants, consistent with the hydrodynamical models of [Joggerst et al. 2009](#)).

4.2. Mean alpha abundance

Using our new 3D non-LTE abundances, we computed the mean alpha-abundance using a simple mean of: [Si/Fe], [Mg/Fe], and [Ca/Fe]. We find that the mean alpha enhancement of SDSS J102915+172927 decreases substantially compared to the original work:

$$[\alpha/\text{Fe}]_{\text{Caffau}} = 0.49 \rightarrow [\alpha/\text{Fe}]_{\text{Lagae}} = -0.11, \quad (5)$$

also shown in Fig. 8. The observed change from alpha-enhanced ($[\alpha/\text{Fe}] \sim 0.4$) to sub-solar alpha abundance is mainly driven by the relative large increase in Fe abundance, compared to the alpha-elements, when going from 1D LTE to 3D non-LTE. [Amarsi et al. \(2022\)](#) found that for warm metal-poor subgiants ($[\text{M}/\text{H}] = -3$) the change in iron abundance, $A(\text{Fe I})_{\text{IDLTE}} - A(\text{Fe I})_{\text{3DnonLTE}}$, can be as large as 0.4 – 0.5 dex. 3D non-LTE abundance changes for the alpha elements are expected to be smaller. Hence, it is not unrealistic to expect similar shifts in alpha-enhancement for other ultra metal-poor stars, shifting the mean alpha-to-iron ratio of the stars shown in Fig. 8 downwards. This would imply that the yields of Pop III supernovae would have produced a lower $[\alpha/\text{Fe}]$ than previously thought. Verification of this claim, however, would require a consistent 3D non-LTE abundance analysis of extremely-metal poor stars ($[\text{Fe}/\text{H}] < -3$).

Our atmospheric models were calculated using alpha elements enhanced by $[\alpha/\text{Fe}] = +0.4$, contrary to our findings that SDSS J102915+172927 has a sub-solar alpha abundance. At these low metallicities H is expected to be the main electron donor such that small changes in metal mass fraction are not expected to significantly impact the atmosphere. To test this, we compared two MARCS models ($T_{\text{eff}} = 5750$ K, $\log g = 4.5$, $[\text{Fe}/\text{H}] = -2.5$, $v_{\text{micro}} = 1$ km/s) that are alpha enhanced ($[\alpha/\text{Fe}] = +0.4$) and alpha normal ($[\alpha/\text{Fe}] = +0.0$), resulting in maximum temperature differences of 15 K throughout the atmosphere.

4.3. Impact on Pop II star formation theories

In the original work, [Caffau et al. \(2012\)](#) concluded that the low carbon upper limit of SDSS J102915+172927 excluded metal-line cooling as a possible mechanism of its star formation. In addition, the total metal mass fraction made SDSS J102915+172927 the most-metal poor star known to date. Using the new 3D non-LTE abundances derived in this work, we first make an estimate of the metal mass fraction Z :

$$\frac{Z}{X} = \sum_{i=\text{element}} \left[10^{A(i)-12} \cdot A_w(i) \right], \quad (6)$$

where $A(i)$ is the abundance and A_w the atomic weight of element i . Subsequently, the normalisation $X + Y + Z = 1$ allows to

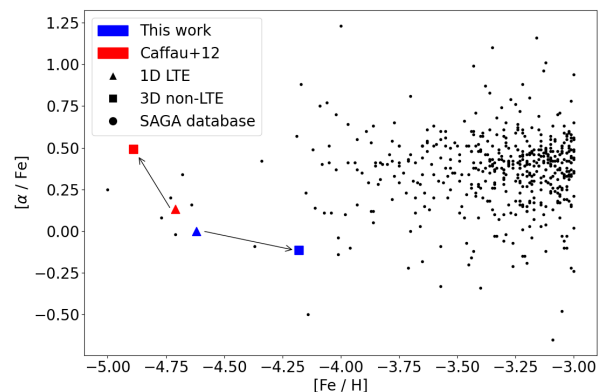


Fig. 8. Similar to Fig. 5 but now for the mean $[\alpha/\text{Fe}]$ abundance.

compute the total metal mass fraction Z :

$$Z = \frac{1 - Y}{1 + \left(\sum_{i=\text{element}} \left[10^{A(i)-12} \cdot A_w(i) \right] \right)^{-1}}, \quad (7)$$

where $Y = 0.2477$ is the primordial He mass fraction ([Peimbert et al. 2007](#)). Using equation 7, we computed two estimates of the mass fraction, Z : one where we restricted the sum over all elements to the species that [Caffau et al. \(2012\)](#) reported (including upper limits), to make a consistent comparison, and one that used the abundances from the best fitting Population III supernova model.

In the first case we included oxygen as $[\text{O}/\text{Fe}] = +0.6$ and Sr with the upper limit as derived in ([Caffau et al. 2012](#)). This results in a total metal content of $Z \approx 1.38 \cdot 10^{-6}$ or $Z/Z_{\odot} \approx 9.8 \cdot 10^{-5}$, that is approximately a factor two higher than the original estimation $Z_{\text{Caffau+12}}/Z_{\odot} = 5 \cdot 10^{-5}$. In the second case, applying the abundances of all species from Li to Zn of the best fitting supernova model, we obtain a value of $Z_{\text{SNe}} \approx 9.1 \cdot 10^{-7}$ or $Z_{\text{SNe}}/Z_{\odot} \approx 6.6 \cdot 10^{-5}$. Even though this estimate includes more elements, the significantly lower N abundance of the supernova model results in an overall lower mass fraction compared to the first case.

Turning now to the possibility of low mass star formation through the mechanism of metal-line cooling. It is theorised ([Bromm & Loeb 2003](#)) that this will only occur if there is a sufficient amount of C and O available in the star-forming cloud. Indeed, metal-line cooling is able to produce low-mass stars if the transition discriminant ([Bromm & Loeb 2003](#); [Frebel et al. 2007](#)):

$$D = \log \left[10^{[\text{C}/\text{H}]} + 0.3 \cdot 10^{[\text{O}/\text{H}]} \right], \quad (8)$$

is greater than $D \geq D_{\text{crit}} = -3.5 \pm 0.2$. Using our new upper limit on C and $[\text{O}/\text{Fe}] = +0.6$, we obtain a transition discriminant $D \leq -3.6 \pm 0.15$ that is marginally comparable to the critical value needed for metal-line cooling, contrary to the original result of [Caffau et al. \(2011\)](#) $D \leq -4.2$. Hence, our result cannot exclude either metal-line cooling or dust-induced fragmentation as the underlying mechanism in the formation of SDSS J102915+172927.

5. Conclusions

In this work we have performed a fully consistent 3D non-LTE abundance analysis of SDSS J102915+172927, known as the

most-metal poor star. For this purpose we employed a tailored 3D atmospheric model using improved stellar parameters and up-to-date atomic data to calculate synthetic spectra. The primary outcome is that the resulting Fe-abundance is +0.57 dex higher than the original value, showcasing the importance of performing consistent 3D non-LTE calculations for ultra metal-poor stars.

The increase in metallicity, together with new upper limits on C and N, has important implications regarding progenitor Pop III properties and low-mass star formation in the early universe. First, we find that the upper limit of the total metal content of the star increases by a factor 2. Together with the increased carbon upper limit, we find that the abundances of the star is consistent with formation both through metal-line cooling and dust-induced fragmentation. Observations with higher S/N are necessary to improve the upper limit on C and to draw stronger conclusions. Secondly, our new 3D non-LTE abundances provide stronger constraints on the mass of the progenitor Pop III star as well as its explosion energy, assuming that SDSS J102915+172927 is mono-enriched, as compared to a 1D LTE analysis. In particular, we find that progenitors with mass $M = 10 - 20 M_{\odot}$ and explosion energy $E_{51} = 0.3 - 3$ are able to reproduce the abundance pattern. The best fit is a Pop III progenitor with mass $M = 10.9 M_{\odot}$ that exploded with energy $E_{51} = 0.6$. These are typical masses and explosion energies for core collapse supernovae (e.g., Müller 2020) and no hypernova model is required. Lastly, the strong increase in $A(\text{Fe})$ coupled with relatively smaller changes in alpha-element abundances changes the status of the star from alpha-enhanced to a star with sub-solar alpha abundance.

Following the conclusion of Nordlander et al. (2017), and in light of upcoming large scale surveys which will provide dozens of new ultra metal-poor stars, it is critical for future studies to apply full 3D non-LTE abundance calculations whenever possible.

Acknowledgements. We thank the anonymous referee for their comments, which have improved the manuscript. We gratefully thank Federico Sestito for providing updated stellar parameters for SDSS J102915.14+172927.9 using Gaia DR3 data. This work has made use of the VALD database, operated at Uppsala University, the Institute of Astronomy RAS in Moscow, and the University of Vienna. CL and KL acknowledge funds from the European Research Council (ERC) under the European Union's Horizon 2020 research and innovation programme (Grant agreement No. 852977). KL also acknowledges funds from the Knut and Alice Wallenberg foundation. AMA gratefully acknowledges support from the Swedish Research Council (VR 2020-03940). LFRD acknowledges support from the Carlsberg Foundation (grant agreement CF19-0649). TTH acknowledges support from the Swedish Research Council (VR 2021-05556). Parts of this research were supported by the Australian Research Council (ARC) Centre of Excellence (CoE) for All Sky Astrophysics in 3 Dimensions (ASTRO 3D), through project number CE170100013. AH was supported, in part, by the ARC CoE for Gravitational Wave Discovery (OzGrave) project number CE170100004 and acknowledges software development support from Astronomy Australia Limited's ADACS scheme (Project IDs AHeger_2022B, AHeger_2023A). This work is based on data obtained from the ESO Science Archive Facility. The computations were performed on resources provided by the Swedish National Infrastructure for Computing (SNIC) at UPPMAX under project SNIC2022/5-351 and PDC under project PDC-BUS-2022-4, and at the Centre for Scientific Computing, Aarhus: <http://phys.au.dk/forskning/cscaa/>.

References

Amarsi, A. M. & Asplund, M. 2017, MNRAS, 464, 264
 Amarsi, A. M., Asplund, M., Collet, R., & Leenaarts, J. 2016a, MNRAS, 455, 3735
 Amarsi, A. M., Liljegren, S., & Nissen, P. E. 2022, arXiv e-prints, arXiv:2209.13449
 Amarsi, A. M., Lind, K., Asplund, M., Barklem, P. S., & Collet, R. 2016b, MNRAS, 463, 1518

Aoki, W., Beers, T. C., Christlieb, N., et al. 2007, ApJ, 655, 492
 Arentsen, A., Placco, V. M., Lee, Y. S., et al. 2022, MNRAS, 515, 4082
 Asplund, M., Amarsi, A. M., & Grevesse, N. 2021, A&A, 653, A141
 Asplund, M., Carlsson, M., & Botnen, A. V. 2003, A&A, 399, L31
 Asplund, M., Grevesse, N., & Sauval, A. J. 2005, in Astronomical Society of the Pacific Conference Series, Vol. 336, Cosmic Abundances as Records of Stellar Evolution and Nucleosynthesis, ed. T. G. Barnes III & F. N. Bash, 25
 Asplund, M., Grevesse, N., Sauval, A. J., & Scott, P. 2009, ARA&A, 47, 481
 Bastian, N., Covey, K. R., & Meyer, M. R. 2010, ARA&A, 48, 339
 Beers, T. C. & Christlieb, N. 2005, ARA&A, 43, 531
 Beers, T. C., Preston, G. W., & Shectman, S. A. 1985, AJ, 90, 2089
 Bergemann, M., Gallagher, A. J., Eitner, P., et al. 2019, A&A, 631, A80
 Bergemann, M., Lind, K., Collet, R., Magic, Z., & Asplund, M. 2012, MNRAS, 427, 27
 Bessell, M. S., Collet, R., Keller, S. C., et al. 2015, ApJ, 806, L16
 Bognar. 2021, Chi-Square Distribution Online Applet, <https://homepage.divms.uiowa.edu/~mbognar/applets/chisq.html>
 Böhm-Vitense, E. 1958, ZAp, 46, 108
 Bonifacio, P., Caffau, E., Spite, M., et al. 2018, Research Notes of the American Astronomical Society, 2, 19
 Bromm, V. & Loeb, A. 2003, Nature, 425, 812
 Bromm, V. & Yoshida, N. 2011, ARA&A, 49, 373
 Caffau, E., Bonifacio, P., François, P., et al. 2011, Nature, 477, 67
 Caffau, E., Bonifacio, P., François, P., et al. 2012, A&A, 542, A51
 Cayrel, R. 1988, in The Impact of Very High S/N Spectroscopy on Stellar Physics, ed. G. Cayrel de Strobel & M. Spite, Vol. 132, 345
 Cayrel, R., Depagne, E., Spite, M., et al. 2004, A&A, 416, 1117
 Chabrier, G. 2003, PASP, 115, 763
 Christlieb, N., Schörck, T., Frebel, A., et al. 2008, A&A, 484, 721
 Clark, P. C., Glover, S. C. O., Klessen, R. S., & Bromm, V. 2011a, ApJ, 727, 110
 Clark, P. C., Glover, S. C. O., Smith, R. J., et al. 2011b, Science, 331, 1040
 Collet, R., Nordlund, Å., Asplund, M., Hayek, W., & Trampedach, R. 2018, MNRAS, 475, 3369
 Dekker, H., D'Odorico, S., Kaufer, A., Delabre, B., & Kotzlowski, H. 2000, in Society of Photo-Optical Instrumentation Engineers (SPIE) Conference Series, Vol. 4008, Optical and IR Telescope Instrumentation and Detectors, ed. M. Iye & A. F. Moorwood, 534-545
 Ezzeddine, R., Frebel, A., & Plez, B. 2017, ApJ, 847, 142
 Ezzeddine, R., Frebel, A., Roederer, I. U., et al. 2019, ApJ, 876, 97
 Frebel, A., Casey, A. R., Jacobson, H. R., & Yu, Q. 2013, ApJ, 769, 57
 Frebel, A., Johnson, J. L., & Bromm, V. 2007, MNRAS, 380, L40
 Frebel, A. & Norris, J. E. 2015, ARA&A, 53, 631
 Gaia Collaboration. 2020, VizieR Online Data Catalog, I/350
 Greif, T. H., Springel, V., White, S. D. M., et al. 2011, ApJ, 737, 75
 Gustafsson, B., Edvardsson, B., Eriksson, K., et al. 2008, A&A, 486, 951
 Hartwig, T., Bromm, V., Klessen, R. S., & Glover, S. C. O. 2015, MNRAS, 447, 3892
 Hartwig, T., Yoshida, N., Magg, M., et al. 2018, MNRAS, 478, 1795
 Hayek, W., Asplund, M., Carlsson, M., et al. 2010, A&A, 517, A49
 Hayek, W., Asplund, M., Collet, R., & Nordlund, Å. 2011, A&A, 529, A158
 Heger, A., Chan, C., Nordlander, T., et al. 2023, PASA, in prep.
 Heger, A. & Woosley, S. E. 2010, ApJ, 724, 341
 Hirano, S., Hosokawa, T., Yoshida, N., et al. 2014, ApJ, 781, 60
 Hosokawa, T., Hirano, S., Kuiper, R., et al. 2016, ApJ, 824, 119
 Hosokawa, T., Omukai, K., Yoshida, N., & Yorke, H. W. 2011, Science, 334, 1250
 Ishigaki, M. N., Tominaga, N., Kobayashi, C., & Nomoto, K. 2014, ApJ, 792, L32
 Ishigaki, M. N., Tominaga, N., Kobayashi, C., & Nomoto, K. 2018, ApJ, 857, 46
 Iwamoto, N., Umeda, H., Tominaga, N., Nomoto, K., & Maeda, K. 2005, Science, 309, 451
 Ji, A. P., Frebel, A., & Bromm, V. 2014, ApJ, 782, 95
 Joggerst, C. C., Almgren, A., Bell, J., et al. 2010, ApJ, 709, 11
 Joggerst, C. C., Woosley, S. E., & Heger, A. 2009, ApJ, 693, 1780
 Keller, S. C., Bessell, M. S., Frebel, A., et al. 2014, Nature, 506, 463
 Klessen, R. S., Glover, S. C. O., & Clark, P. C. 2012, MNRAS, 421, 3217
 Kroupa, P. 2002, Science, 295, 82
 Kurucz, R. L. 2008, Robert L. Kurucz on-line database of observed and predicted atomic transitions
 Kurucz, R. L. 2016, Robert L. Kurucz on-line database of observed and predicted atomic transitions
 Lai, D. K., Bolte, M., Johnson, J. A., et al. 2008, ApJ, 681, 1524
 Leenaarts, J. & Carlsson, M. 2009, in Astronomical Society of the Pacific Conference Series, Vol. 415, The Second Hinode Science Meeting: Beyond Discovery-Toward Understanding, ed. B. Lites, M. Cheung, T. Magara, J. Mariska, & K. Reeves, 87
 Limongi, M. & Chieffi, A. 2012, ApJS, 199, 38
 Lind, K., Amarsi, A. M., Asplund, M., et al. 2017, MNRAS, 468, 4311
 Lind, K., Asplund, M., Barklem, P. S., & Belyaev, A. K. 2011, A&A, 528, A103

- Ludwig, H. G., Bonifacio, P., Caffau, E., et al. 2008, *Physica Scripta* Volume T, 133, 014037
- Ludwig, H. G. & Steffen, M. 2013, *Memorie della Societa Astronomica Italiana Supplementi*, 24, 53
- Magg, M., Klessen, R. S., Glover, S. C. O., & Li, H. 2019, *MNRAS*, 487, 486
- Magg, M., Nordlander, T., Glover, S. C. O., et al. 2020, *MNRAS*, 498, 3703
- Magic, Z., Collet, R., Asplund, M., et al. 2013, *A&A*, 557, A26
- Mallinson, J. W. E., Lind, K., Amarsi, A. M., et al. 2022, arXiv e-prints, arXiv:2210.08880
- Mashonkina, L., Jablonka, P., Sitnova, T., Pakhomov, Y., & North, P. 2017, *A&A*, 608, A89
- Meléndez, J., Casagrande, L., Ramírez, I., Asplund, M., & Schuster, W. J. 2010, *A&A*, 515, L3
- Mihalas, D., Dappen, W., & Hummer, D. G. 1988, *ApJ*, 331, 815
- Müller, B. 2020, *Living Reviews in Computational Astrophysics*, 6, 3
- Nomoto, K., Kobayashi, C., & Tominaga, N. 2013, *ARA&A*, 51, 457
- Nordlander, T., Amarsi, A. M., Lind, K., et al. 2017, *A&A*, 597, A6
- Nordlander, T. & Lind, K. 2017, *A&A*, 607, A75
- Nordlund, A. 1982, *A&A*, 107, 1
- Nordlund, A. & Galsgaard, K. 1995, *stagger-code*
- Nordlund, Å., Stein, R. F., & Asplund, M. 2009, *Living Reviews in Solar Physics*, 6, 2
- Omukai, K., Tsuribe, T., Schneider, R., & Ferrara, A. 2005, *ApJ*, 626, 627
- Peimbert, M., Luridiana, V., & Peimbert, A. 2007, *ApJ*, 666, 636
- Piskunov, N. E., Kupka, F., Ryabchikova, T. A., Weiss, W. W., & Jeffery, C. S. 1995, *A&AS*, 112, 525
- Placco, V. M., Frebel, A., Beers, T. C., & Stancliffe, R. J. 2014, *ApJ*, 797, 21
- Placco, V. M., Frebel, A., Lee, Y. S., et al. 2015, *ApJ*, 809, 136
- Ryabchikova, T., Piskunov, N., Kurucz, R. L., et al. 2015, *Phys. Scr*, 90, 054005
- Rybicki, G. B. & Hummer, D. G. 1992, *A&A*, 262, 209
- Sbordone, L., Bonifacio, P., Caffau, E., et al. 2010, *A&A*, 522, A26
- Schneider, R., Ferrara, A., Salvaterra, R., Omukai, K., & Bromm, V. 2003, *Nature*, 422, 869
- Schneider, R., Omukai, K., Bianchi, S., & Valiante, R. 2012a, *MNRAS*, 419, 1566
- Schneider, R., Omukai, K., Limongi, M., et al. 2012b, *MNRAS*, 423, L60
- Sestito, F., Longeard, N., Martin, N. F., et al. 2019, *MNRAS*, 484, 2166
- Sitnova, T. M., Mashonkina, L. I., Ezzeddine, R., & Frebel, A. 2019, *MNRAS*, 485, 3527
- Skartlien, R. 2000, *ApJ*, 536, 465
- Spite, F. & Spite, M. 1982, *A&A*, 115, 357
- Stacy, A. & Bromm, V. 2013, *MNRAS*, 433, 1094
- Stacy, A., Bromm, V., & Lee, A. T. 2016, *MNRAS*, 462, 1307
- Stein, R. F. & Nordlund, Å. 1998, *ApJ*, 499, 914
- Suda, T., Katsuta, Y., Yamada, S., et al. 2008, *PASJ*, 60, 1159
- Susa, H. 2013, *ApJ*, 773, 185
- Susa, H., Hasegawa, K., & Tominaga, N. 2014, *ApJ*, 792, 32
- Tominaga, N., Iwamoto, N., & Nomoto, K. 2014, *ApJ*, 785, 98
- Tominaga, N., Umeda, H., & Nomoto, K. 2007, *ApJ*, 660, 516
- Trampedach, R., Asplund, M., Collet, R., Nordlund, Å., & Stein, R. F. 2013, *ApJ*, 769, 18
- Vickers, T. J. 2000, *Applied Spectroscopy*, 54, 162A
- Wang, E. X., Nordlander, T., Asplund, M., et al. 2021, *MNRAS*, 500, 2159

Appendix A: $\bar{\chi}^2$ -values of the upper limit determination

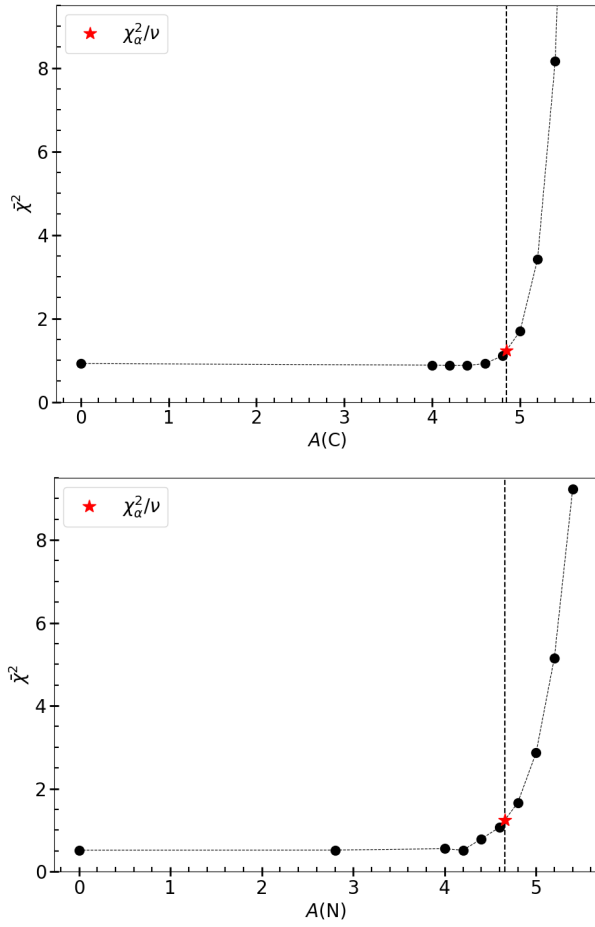


Fig. A.1. Overview of the $\bar{\chi}^2$ values corresponding to the different synthetic spectra of CH and NH. The red star represents the interpolated abundance where $\bar{\chi}^2 \approx \chi^2_{\alpha}/\nu$, also highlighted with a vertical dashed line.

Appendix B: Linelist

Table B.1. Equivalent widths of the measured spectral lines together with respective oscillator strength ($\log gf$) and lower level excitation potential (E_{low}). References to the atomic data are given in § 2.3.

Ion	λ [Å]	W_{UVES} [mÅ]	$\log gf$	E_{low} [eV]
Li I	6707.6000	22 ± 2	0.174	0.000
Na I	5891.6000	22 ± 2	-0.194	0.000
Mg I	3832.29	28 ± 4	-0.339	2.712
	0.138	...
Mg I	3838.29	36 ± 4	-1.515	2.717
...	0.409	...
...	-0.339	...
Mg I	5172.7140	11 ± 1	-0.363	2.712
Mg I	5183.6340	18 ± 2	-0.168	2.717
Al I	3961.5000	22 ± 2	-0.333	0.014
Si I	3905.5460	17 ± 2	-1.040	1.909
Ca I	4226.7500	22 ± 2	0.244	0.000
Ca II	8542.0900	93 ± 3	-0.463	7.813
Ca II	8662.1410	77 ± 3	-0.723	7.806
Ti II	3372.7926	36 ± 9	0.280	0.012
Ti II	3361.2121	37 ± 8	0.410	0.028
Ti II	3349.4022	39 ± 11	0.540	0.049
Fe I	4383.5444	31 ± 2	0.208	0.859
Fe I	4325.7615	11 ± 2	0.006	1.608
Fe I	4307.9016	12 ± 2	-0.072	1.557
Fe I	4271.7599	18 ± 2	-0.173	1.485
Fe I	4202.0288	10 ± 2	-0.689	1.485
Fe I	4071.7375	13 ± 2	-0.008	1.608
Fe I	4063.5936	20 ± 2	0.062	1.557
Fe I	4045.8119	28 ± 2	0.284	1.485
Fe I	3930.2963	26 ± 2	-1.491	0.087
Fe I	3927.9194	19 ± 2	-1.522	0.110
Fe I	3922.9112	19 ± 2	-1.626	0.052
Fe I	3920.2574	8 ± 2	-1.734	0.121
Fe I	3899.7070	19 ± 2	-1.515	0.087
Fe I	3895.6559	14 ± 2	-1.668	0.110
Fe I	3886.2818	39 ± 2	-1.055	0.052
Fe I	3878.5728	32 ± 2	-1.379	0.087
Fe I	3878.0177	10 ± 2	-0.896	0.958
Fe I	3859.9110	61 ± 2	-0.698	0.000
Fe I	3856.3711	26 ± 2	-1.280	0.052
Fe I	3841.0475	11 ± 2	-0.044	1.608
Fe I	3840.4372	17 ± 2	-0.497	0.990
Fe I	3834.2221	15 ± 2	-0.269	0.958
Fe I	3827.8222	12 ± 2	0.094	1.557
Fe I	3825.8805	36 ± 2	-0.024	0.915
Fe I	3824.4432	29 ± 2	-1.342	0.000
Fe I	3820.4249	49 ± 2	0.157	0.859
Fe I	3815.8396	23 ± 2	0.237	1.485
Fe I	3812.9642	5.3 ± 1.5	-1.047	0.958
Fe I	3787.8799	11 ± 2	-0.838	1.011
Fe I	3767.1914	12 ± 2	-0.382	1.011
Fe I	3763.7886	27 ± 2	-0.221	0.990
Fe I	3758.2326	37 ± 4	-0.005	0.958
Fe I	3749.4848	32 ± 4	0.190	0.915
Fe I	3748.2618	30 ± 4	-1.008	0.110
Fe I	3745.8991	21 ± 4	-1.336	0.121
Fe I	3745.5608	50 ± 4	-0.767	0.087
Fe I	3737.1312	57 ± 4	-0.572	0.052
Fe I	3727.6187	17 ± 4	-0.601	0.958
Fe I	3722.5627	26 ± 4	-1.280	0.087
Fe I	3719.9344	63 ± 4	-0.424	0.000
Fe I	3705.5654	23 ± 4	-1.321	0.052

Table B.1. continued

Ion	λ [Å]	W_{UVES} [mÅ]	$\log gf$	E_{low} [eV]
Fe I	3647.8422	32 ± 3	-0.141	0.915
Fe I	3631.4629	33 ± 3	0.0001	0.958
Fe I	3618.7675	35 ± 4	-0.003	0.990
Fe I	3608.8589	28 ± 4	-0.090	1.011
Fe I	3586.9843	14 ± 3	-0.795	0.990
Fe I	3581.1927	62 ± 4	0.415	0.859
Fe I	3565.3787	26 ± 4	-0.133	0.958
Fe I	3490.5735	30 ± 4	-1.105	0.052
Fe I	3475.4499	29 ± 4	-1.054	0.087
Fe I	3465.8603	26 ± 5	-1.192	0.110
Fe I	3440.9883	53 ± 5	-0.958	0.052
Fe I	3440.6054	53 ± 6	-0.673	0.000
Ni I	3619.3910	20 ± 4	-0.137	0.423
Ni I	3524.5360	50 ± 6	-0.157	0.025
Ni I	3510.3320	11 ± 4	-0.807	0.212
Ni I	3492.9570	27 ± 6	-0.407	0.109
Ni I	3461.6540	37 ± 9	-0.517	0.025
Ni I	3458.4600	23 ± 6	-0.377	0.212
Ni I	3446.2590	28 ± 7	-0.547	0.109
Ni I	3414.7650	46 ± 8	-0.167	0.025
Ni I	3392.9860	31 ± 8	-0.677	0.025
CH	G-band 4300			
NH	NH-band 3360			